# Bulk and surface electronic structure of NiBi₃

Cris Adriano [1,2,*], Kyungchan Lee,[2,3,†] Yevhen Kushnirenko,[2] Benjamin Schrunk,[3] Kevin R. Pakuszewski [1],
Lin-Lin Wang [3], Sergey L. Bud'ko,[2,3] Paul C. Canfield,[2,3] and Adam Kaminski[2,3]

[1]*Instituto de Física "Gleb Wataghin," Universidade Estadual de Campinas, UNICAMP, 13083-859 Campinas, Sao Paulo, Brazil*
[2]*Department of Physics and Astronomy, Iowa State University, Ames, Iowa 50011, USA*
[3]*Ames Laboratory, Iowa State University, Ames, Iowa 50011, USA*

We present a high-resolution, angle-resolved photoemission spectroscopy study of the normal electronic state of the superconducting NiBi₃. Our experimental results show a complex Fermi surface structure with many sheets along the $\Gamma$-$X$ and $\Gamma$-$Y$ directions of the Brillouin zone. The band structure presents a topological surface state (TSS) at the high symmetry $\Gamma$ point with a surface Dirac point at the energy $-0.185$ eV. The Dirac-like cone presents a linear dispersion along $k_x$ while it presents saddle-like states along $k_y$ located in the vicinity of the surface Dirac point. Our results are in good agreement with results of density functional theory band structure calculations. We also discuss the topological band structure of the NiBi₃ compound.

## I. INTRODUCTION

The search for novel topological phases in materials has led to the study of several binary compounds containing bismuth, since this element has strong spin-orbit coupling (SOC), which can be considered as one of the ingredients for the occurrence of exotic topological phases [1–3]. Recently, it was shown that elemental Bi is a strong topological insulator with nonvanishing weak indices [4–6]. Furthermore, one of the first three-dimensional topological insulators was identified in Bi$_{1-x}$Sb$_x$ alloys [5,7]. Therefore, it is expected that studies of compounds containing bismuth will keep attracting attention of researchers focused on discovery of new topological phases [1]. In particular, the investigation of topological phases in superconducting materials is motivated by the search for materials and/or heterostructures that could host the protected zero-energy Majorana surface states [8], which are claimed to have important applications in quantum computing [8–10].

Alloys of Ni and Bi are widely studied due to their industrial applications, such as lead-free solders [11,12] and lately as thermal interface materials [13]. According to the Ni-Bi phase diagram, there are two intermetallic phases in this system: NiBi, which has a crystal structure that is hexagonal belonging to the P6$_3$/*mmc* space group and that becomes a superconductor at around 4.3 K; and NiBi₃, which is orthorhombic and belongs to the P*nma* space group [14]. NiBi₃ is known to be a type-II superconductor with a critical temperature of about 4.1 K [14–17]. An earlier work had suggested the coexistence of superconductivity and ferromagnetism [18]; however, later the ferromagnetism was attributed to the amorphous Ni impurities in the compound [19]. Even more recently, Andreev reflection spectroscopy was performed to confirm that the bulk NiBi₃ is a singlet *s*-wave superconductor

with no magnetic order [17]. Besides, the superconductivity was also studied as a function of pressure, which suggested that NiBi₃ is a conventional, electron-phonon mediated BCS superconductor [15].

In this work, we present results of an investigation of the band structure of single-crystalline NiBi₃ using high-resolution laser-based angle-resolved photoemission spectroscopy (ARPES) measurements and density functional theory (DFT) calculations. The crystal structure and Brillouin zone (BZ) for NiBi₃ are shown in Figs. 1(a) and 1(b) respectively. NiBi₃ is centrosymmetric with lattice parameters $a = 8.878$ Å, $b = 4.102$ Å, and $c = 11.479$ Å [16]. Ni atoms are positioned in a zigzag linear chain along the $b$ axis while Bi form octahedral chain along the $b$ axis [14]. There is one crystallographic Ni site and three Bi sites per unit cell. There is a van der Waals–like gap between layers perpendicular to the $c$ axis that exposes Bi layers containing all three Bi sites. The crystals are soft and needle-shaped and have dimensions of about $5 \times 0.2 \times 0.2$ mm³ for which the longest needle axis is the crystallographic $b$ axis [15]. We were able to perform experiments along the $a$-$b$ crystallographic plane and then reconstruct the somewhat complicated Fermi surface (FS) of the compound along $k_x$-$k_y$ in the momenta space. Interestingly, the band structure shows a surface state centered at the $\Gamma$ point and a Dirac-like node at energy $-0.185$ eV.

## II. METHODS

Single crystals of NiBi₃ were grown by a flux-growth technique out of excess Bi [15]. Elemental Ni and Bi (both 99.99% pure from Alfa Aesar), with an initial molar ratio of 1:9, were placed in alumina Canfield crucible set [20] and sealed in a quartz tube under a partial Ar pressure ($\approx$1/5 atm). The ampoule was heated up to 1000 °C and dwelled for 3 h. It was cooled rapidly to 600 °C (3 h), dwelled for 3 h, and then slowly cooled to 320 °C over 40 h. The excess of Bi was decanted using a centrifuge [15].

---

*cadriano@unicamp.br
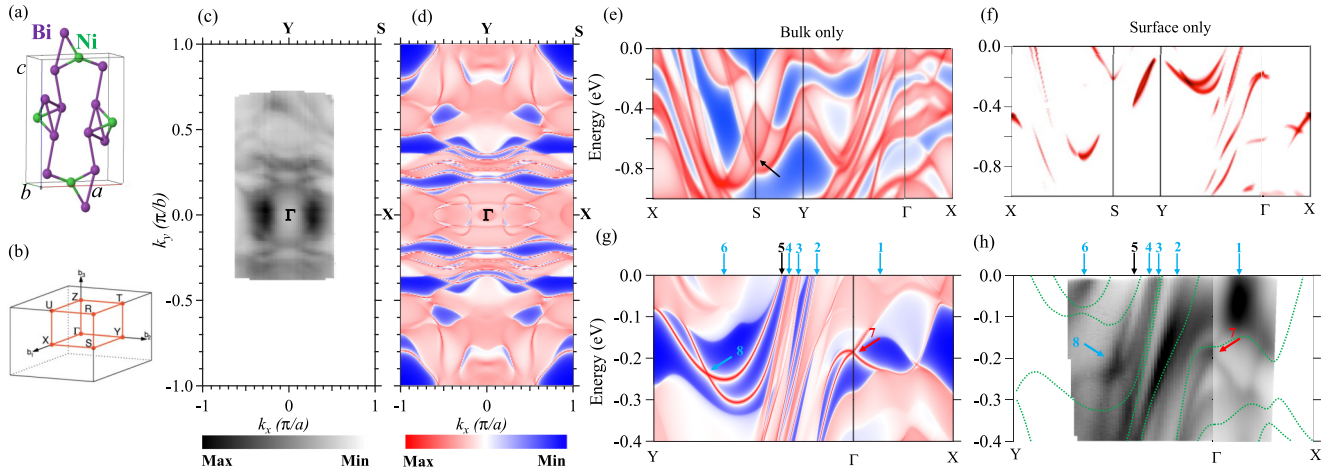†Present address: Julius-Maximilians-Universität, Physikalisches Institut Am Hubland 97074 Würzburg, Germany.

FIG. 1. (a) Crystal structure of NiBi₃ [14], Ni atoms are labeled in green and Bi atoms in purple; (b) Brillouin zone of NiBi₃; (c) experimental Fermi surface perpendicular to (001) integrated within 10 meV of the chemical potential measured at 5 K and photon energy of 6.7 eV; (d) calculated Fermi surface; calculated band dispersion along the main directions of the BZ showing (e) the bulk bands and (f) the SS's; and band dispersion map along Γ-X and Γ-Y directions of the BZ in a −0.4 eV window for (g) bulk and SS's dispersion and (h) ARPES data measured at 5 K and 6.7 eV.

The ARPES experiments were performed in a laser-based system with a hemispherical electron-energy analyzer (Scienta-Omicron DA30) and a tunable ultraviolet laser light source that consists of a picosecond Ti:sapphire oscillator and fourth harmonic generator [21]. All measurements were carried out with a constant photon energy of 6.7 eV, except for data in Fig. 2(b) that were measured using 6.2 eV. The energy resolution was set to 1 meV at 5 K and the angular resolution was set to 0.05°. The size of the photon beam on the sample was of the order of 15 μm² and samples were cleaved in situ perpendicular to the (001) direction at a base pressure of ≈2 × 10⁻¹¹ Torr. Given that the base temperature for our cold finger running in continuous mode is around 4.0 K, we could not measure any potential shifts or partial gap openings in this $T_c$ = 4.1 K superconductor. Instead we performed the measurements at low temperature, normal state just above $T_c$, at 5.0 K.

Band structures of NiBi₃ have been calculated using DFT [22,23] and Perdew-Burke-Ernzerhof (PBE) [24] as exchange-correlation functional with SOC effect included. All DFT calculations have been performed in VASP [25,26] with a plane-wave basis set and projector augmented wave [27] method. We used the orthorhombic unit cell of 16 atoms with a Γ-centered Monkhorst-Pack [28] (5 × 12 × 4) k-point mesh with a Gaussian smearing of 0.05 eV. The kinetic energy cutoff was 270 eV. A tight-binding model based on maximally localized Wannier functions [29,30] was constructed to reproduce closely the bulk band structure including SOC in the range of $E_F$ ± 1 eV with Ni $sd$ and Bi $p$ orbitals. Then 2D FSs and spectral functions of the semi-infinite surface were calculated with the surface Green's function methods [31,32] as implemented in WANNIERTOOLS [33].

## III. RESULTS AND DISCUSSION

We start our discussion by presenting the broad overview of the band structure and FS reconstruction for NiBi₃.

Figure 1(c) shows the experimental FS perpendicular to (001) measured at 6.7 eV in which the ARPES intensity was integrated within 10 meV of the chemical potential. High-intensity areas present the contours of the FS sheets. Figure 1(d) shows the calculated 2D bulk and surface contributions to the FS. The calculated DFT band structure is presented along the main symmetry directions of the BZ in a 1 eV energy window and represents the projection along $k_z$ direction of the bulk bands in Fig. 1(e) and the surface states (SS) that are predicted to be present in NiBi₃ in Fig. 1(f). Figure 1(g) shows in detail the calculated band structure along Y-Γ-X directions for bulk and SS's together, while the experimental data for the same directions is presented in Fig. 1(h). The dashed green lines on top of Fig. 1(h) represent the band structure calculated for Y-Γ-X directions. Note that Figs. 1(d)–1(g) show the calculated dispersion projected along the $k_z$ direction, while in Figs. 1(c) and 1(h) the data were taken in low photon energy, which has dispersion in $k_z$ of about 10%. We compare the ARPES data to results of semi-infinite surface DFT calculations as these capture both bulk and surface contributions that are both present in ARPES measurement. We note that these DFT calculations fully project bulk bands along the $k_z$ direction, while ARPES measurements have a degree of $k_z$ selectivity (i.e., ARPES signal is an average over limited range of $k_z$'s centered at a particular value of $k_z$ determined by the photon energy). One therefore would not expect perfect agreement between ARPES and semi-infinite surface DFT results for the bulk bands. There should be a fair agreement with respect to surface states, which are main focus of this work.

The reconstructed FS around the Γ point consists of two high-intensity areas centered at $k_x = \pm 0.3\ \pi/a$ along Γ-X direction. Its dispersion can be seen as a bright and broad dispersion along the same direction in Fig. 1(h), arrow 1. According to the calculations, around $k_x = \pm 0.3\ \pi/a$, there are two bulk hole pockets that are degenerate only along
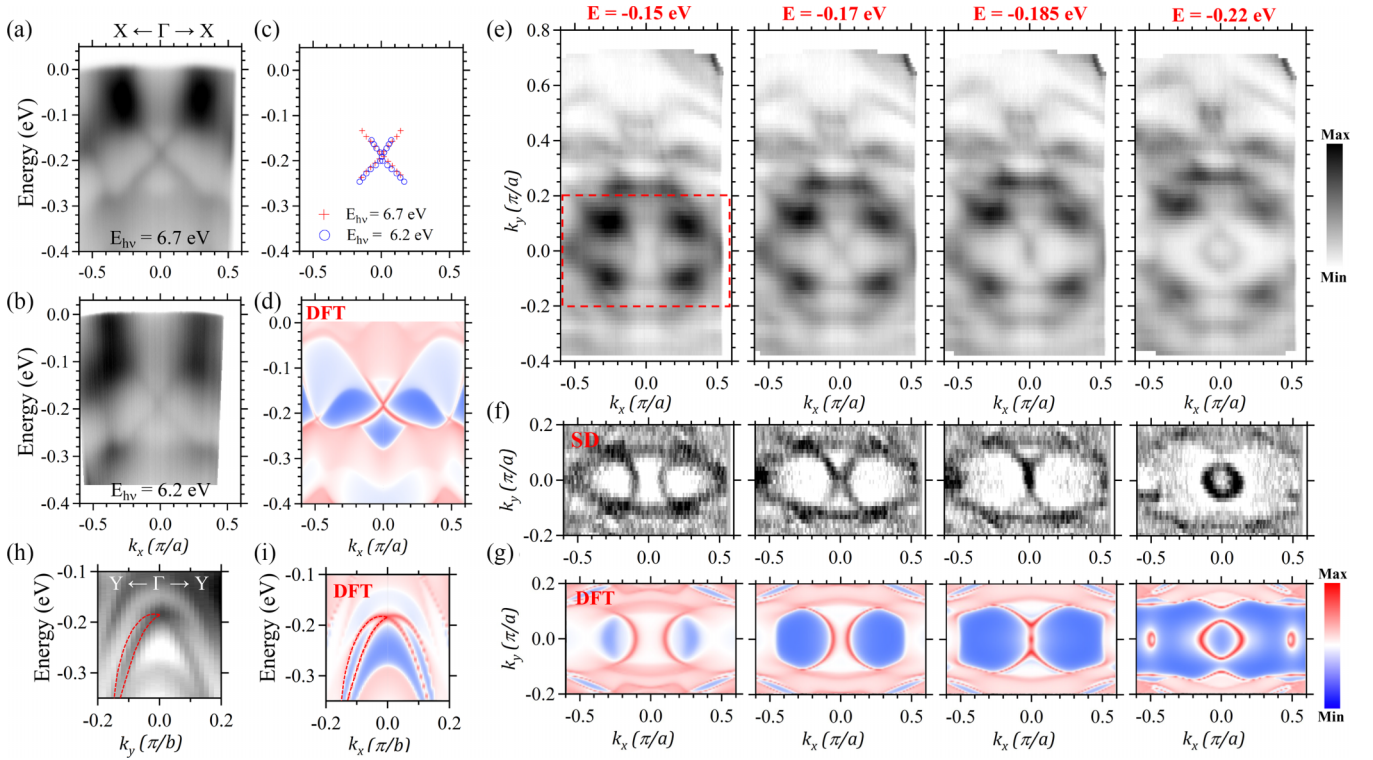
FIG. 2. ARPES dispersion map along $\Gamma$-$X$ measured using incident photon energy of (a) 6.7 eV and (b) 6.2 eV; (c) points obtained by fitting Gaussian peaks to the MDC's of the data shown in panels (a) and (b); (d) DFT calculations in the same energy and momentum window along $\Gamma$-$X$; (e) constant energy contour plots for different values of the binding energy showed on top of each panel; (f) second derivatives (SD) and (g) DFT calculations of the area enclosed in the dashed red rectangle in panel (d) ($-0.15$ eV) of the constant energy contour plots; and dispersion map along $\Gamma$-$Y$ (h) ARPES measurements and (i) DFT calculations.

the high-symmetry $Z$-$U$ direction (see discussion below). Off this high-symmetry direction, the degeneracy is lifted and the pockets appear in two concentric roundish triangles as seen from the bulk band projection on (001). As the inner potential of NiBi$_3$ is unknown, we cannot predict the exact position along $\Gamma$-$Z$ that is being probed. We chose to show on top of the experimental data the calculated $\Gamma$ cut as this presents the greatest agreement. However, the pocket at $0.3\,\pi/a$ suggests that we are not exactly at the $\Gamma$ cut.

Along the $\Gamma$-$Y$ direction, the measured FS presents a broad structure around $0.15$–$0.20\,\pi/b$ [arrow 2 in Figs. 1(g) and 1(h)], followed by three Fermi sheets very close together between $0.25$ and $0.35\,\pi/b$ [region pointed by arrows 3 and 4] and a fourth one at $\approx 0.4\,\pi/b$ [arrows 5 in Figs. 1(g) and 1(h)] and then a pocket at $\approx 0.65\,\pi/b$ [arrow 6 in Figs. 1(g) and 1(h)]. The experimental FS pockets above $k_y = 0.6\,\pi/b$ are not centered with respect to $\Gamma$ and appear somehow distorted. This can be explained because NiBi$_3$ single crystals have a form of soft needles that can twist along the $b$ axis. At these higher values of $k_y$ a small shift of incident photon beam due to tiny misalignment can slightly alter the actual $k_y$ value during momentum scans. The calculated DFT band structure suggests that the width of dispersion marked by arrow 2 in Figs. 1(g) and 1(h) comes from the coexistence of a bulk band and a SS in this region, which makes the dispersion broad. The regions market by arrows 3 and 4 possibly correspond to two bulk bands and one SS respectively. Arrow 5, in black, shows a SS which appears in slightly smaller values of $k_y$

in the calculated DFT dispersion when compared with the experimental data. For these regions market from arrows 2–5, ARPES data cannot solve all the bands that are suggested to be present from the DFT calculation. The band that crosses the Fermi level at $\approx 0.65\,\pi/b$ is marked by arrow 6 and forms an electron pocket at the FS.

Remarkably, the experimental band structure shows a Dirac-like cone state centered at the $\Gamma$ point, which characterizes a topological surface state (TSS), with a surface Dirac point at $-0.185$ eV. This is in agreement with the results of the DFT calculations [red arrow 7 in Figs. 1(g) and 1(h)]; see discussion of the topological nature in Fig. 4. By following the bands marked by 4 and 5 along $k_y$, the DFT predicts a Rashba-like split surface state, but current data are not sufficient to confirm it, as it can be seen by arrow 8 in both calculated and experimental panels. In addition, the calculated bulk band structure shows a Dirac nodal loop at the S point [black arrow in Fig. 1(e)], and the origin will be discussed below.

Overall, the data show a coexistence of 2D bands and broader bulk bands with a good agreement observed for several features; see, for instance, that arrows 1–4 and 6 are positioned in the same momentum values in both experimental and calculated band maps. Some features appear in slightly different regions of the map when we compare the observed and calculated data, which suggests that at 6.7 eV the probed $k_z$ may be off of a high symmetry point.

To confirm the nature of the TSS at $\Gamma$, we studied photon energy dependence of ARPES data. Figures 2(a) and 2(b)
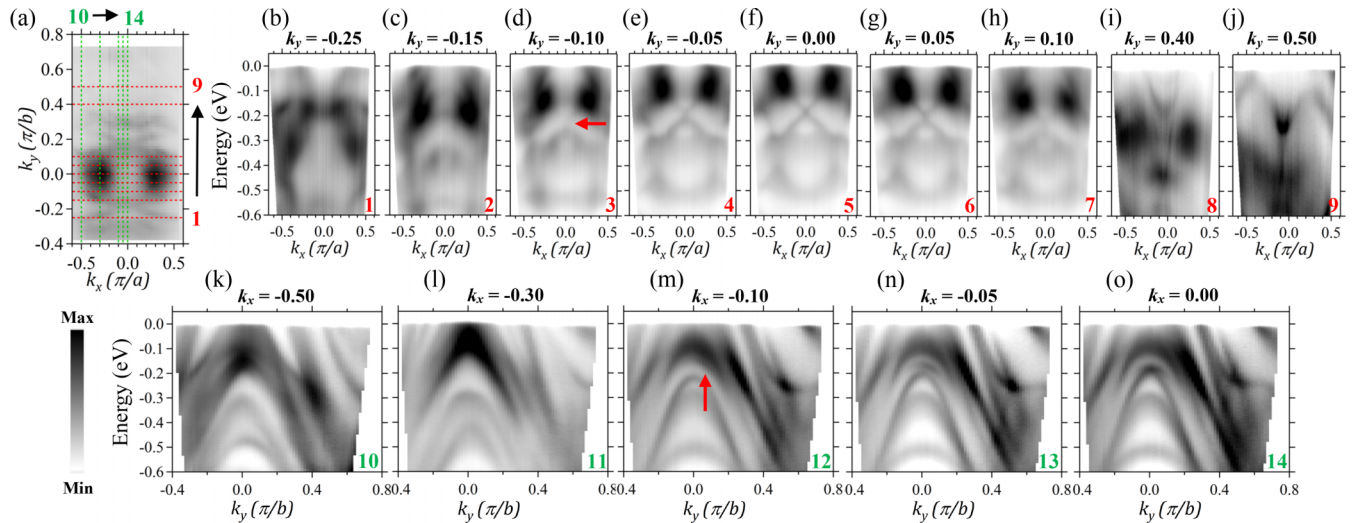
FIG. 3. (a) FS map showing the position for which band dispersion maps were taken along (b)–(j) $k_x$ cuts $1 \rightarrow 9$ represented as dashed horizontal red lines; and (k)–(o) $k_y$ cuts $10 \rightarrow 14$ represented as dashed vertical green lines. The corresponding value of momentum is marked on the top of each figure. Red arrows in panels (d) and (m) show the onset of the top branch of the TSS.

show the ARPES dispersion map along $k_x$ in a 0.4 eV energy window for $k_y = 0 \, \pi/b$ for 6.7 and 6.2 eV incident photon energy, respectively. In this range of momentum, we can identify in both cases the bright bands in the vicinity of $E_F$ [arrow 1 in Fig. 1(h)] and the Dirac-like cone that appears as an $X$-shaped linearly dispersing state along $\Gamma$-$X$. Figure 2(c) shows dispersion points that were obtained by fitting the momentum dispersive curves (MDC's) for different energies using a Gaussian function for the TSS region of the maps shown in Figs. 2(a) and 2(b) for 6.7 (red crosses) and 6.2 eV (blue circles). Notwithstanding, the linear crossing dispersion of the states at intermediate energy ($-0.12$ to $-0.26$ eV) around $\Gamma$ is unchanged with respect to the photon energy, supporting the two-dimensional nature of this state. Figure 2(d) shows the results of the DFT calculations for the same energy and momentum window along $\Gamma$-$X$. Although there is overall good agreements between our data and the DFT calculations, it is worth noting that experimentally the Dirac-like cone is much straighter, or cone-like, than in the calculations.

We now focus on the dispersion of the TSS, which does not present a typical Dirac-like dispersion. Figure 2(e) shows the constant energy contour plots centered at $\Gamma$ for different energies marked on the top of each panel. Moving from the Fermi level toward higher energies, the high-intensity areas centered at $k_x = \pm 0.3 \, \pi/a$ start to split along $k_y$ as we can see for $-0.15$ eV. At this energy, which is 0.035 eV above the Dirac point, it is possible to start seeing the onset of the upper branch of the TSS at around $k_x \pm 0.1 \, \pi/a$ and $k_y = 0 \, \pi/b$ that will move closer to each other as the energy increases (see $-0.17$ eV) until they touch at $-0.185$ eV in a surface Dirac point. To better follow the evolution of the states as a function of the energy near $\Gamma$, Fig. 2(f) shows the second derivative (SD) of the raw data and Fig. 2(g) shows the DFT calculations of the constant energy contour plots enclosed in the dashed red rectangle of Fig. 2(e) ($-0.15$ eV panel) for the same energies of the original data. From Fig. 2(f), it is clear that the upper branch of the TSS does not form a circular pocket therefore, not characterizing a cone, but a concave lens-shape separated

along $k_y$. Below the Dirac point, we can see a circular pocket that forms a cone (panel $-0.22$ eV). As a function of the momentum, the Dirac-like cone presents a nonconventional dispersion, where the TSS shows a linear $X$-shape dispersion along $\Gamma$-$X$ as presented in Fig. 2(a). Along $\Gamma$-$Y$ the band dispersion reveals a saddle-like topological surface state in Fig. 2(h) with an almost flat region that collapses into a Dirac point at $-0.185$ eV. The two parabolic states have maxima at $k_y \pm 0.03 \, \pi/b$ and $-0.175$ eV. The calculated DFT predicts this saddle-like state, as can be seen in Fig. 2(i). While the inner branches will form the Dirac-like cone, the outermost branches will merge with the bulk bands. The dashed red line on top of the experimental band dispersion on the left side was taken directly from the calculated DFT as shown. The occurrence of a saddle state could cause a van Hove singularity (divergence of the density of states) in NiBi$_3$. Interestingly, when this kind of increased density of states is close to the Fermi level, it enhances the electron correlations which might lead to emergence of exotic phenomena [34], such as topological superconductivity [35]. Similar results were found for the triclinic weak topological insulator RhBi$_2$ that presents Dirac surface state at the $Z$ point. RhBi$_2$ shows an $X$-shape linear dispersion along $k_z$ while along the perpendicular direction $k_y$ the upper bands present two parabolas with positive curvature that gives rise to two local minima in energy identified as a two saddle points close to $E_F$ ($\approx 80$ meV). For RhBi$_2$ the ARPES data and calculations based on the effective model showed that the saddle points are related to a van Hove singularity [36].

To explore in details the band structure of the compound, Fig. 3(a) shows the FS of NiBi$_3$ in which we mark the cuts for which we analyze the evolution of the band structure. Cuts $1 \rightarrow 9$ (dashed horizontal red lines) were taken along $k_x$ and are presented in Figs. 3(b)–3(j), with the corresponding value of $k_y$ marked on top of each figure. It is possible to follow the behavior of the bulk bands that form the bright areas centered at $k_x = \pm 0.3 \, \pi/a$. The nontrivial dispersion of the top branch of the TSS is also evident in Figs. 3(c) and 3(d). At $k_y = -0.15$ $\pi/b$ and energy around $-0.35$ eV, we can see a parabolic-like
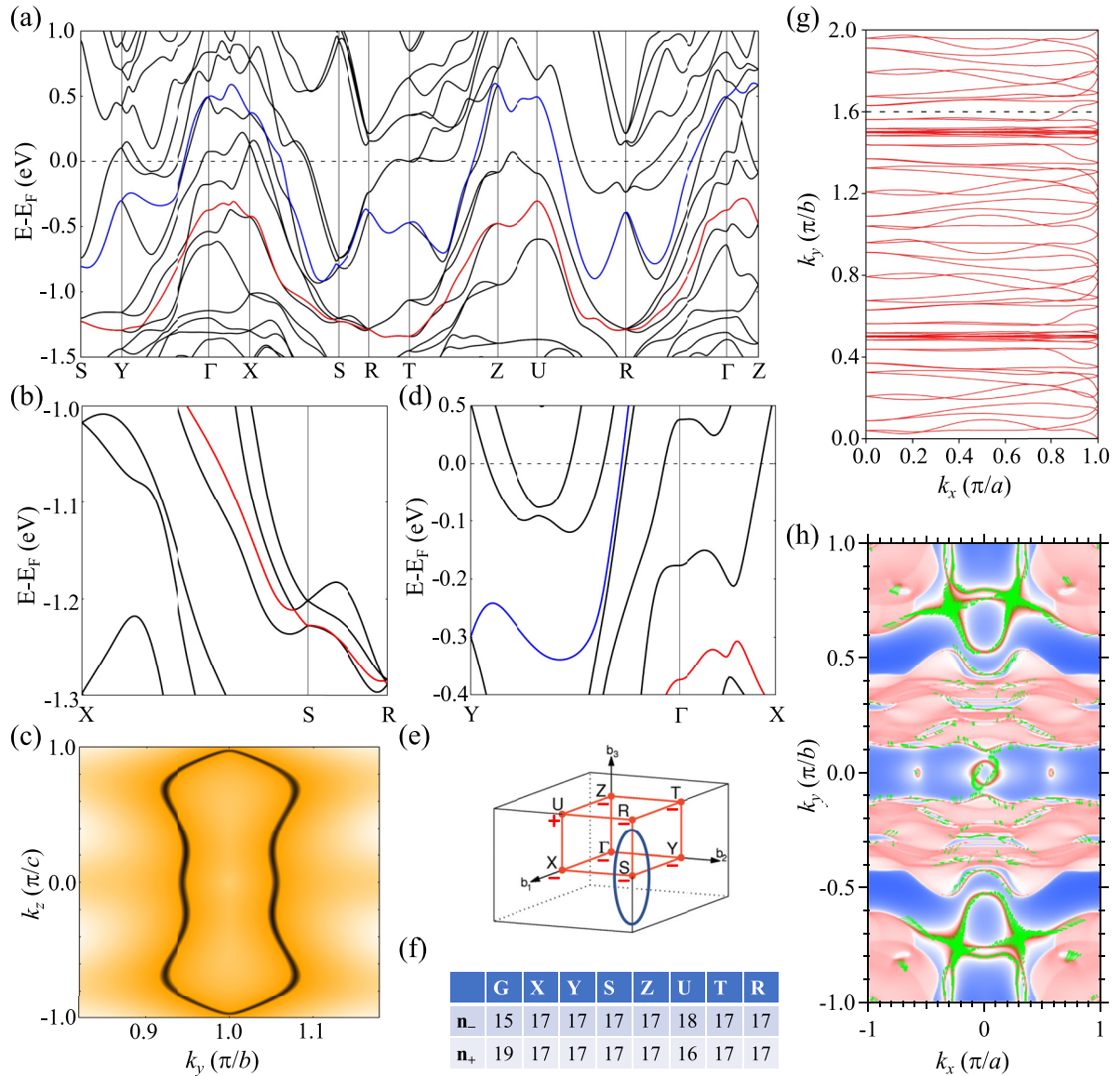
FIG. 4. (a) NiBi$_3$ bulk band structure calculated in PBE+SOC with the bands $N$ and $N - 8$ highlighted in blue and red, respectively, where $N$ is the number of electron and the top valence band according to simple band filling. (b) Band structure zoomed along the $X$-$S$-$R$ direction. (c) Contour of the bulk band gap on the $k_x = 1.0 \, \pi/a$ plane showing the Dirac nodal loop protected by the glide plane. (d) Band structure zoomed along the $Y$-$\Gamma$-$X$ direction. (e) Product of parity eigenvalues at the TRIM labeled in BZ with the corresponding values ($n_+$ and $n_-$) listed in panel (f). (g) Wilson loop of Wannier charge centers on the gapped $k_z = 1.0 \, \pi/c$ plane. The horizontal dashed line shows an odd number of crossings. (h) Spin texture (green arrows) decorated isoenergetic surface perpendicular to (001) at $-0.21$ eV.

band which is a transversal cross section of the cone that forms the lower branch of the TSS, but no bands are present at the top part of the TSS in this cut (except for the bulk bands closer to the Fermi level). As the $k_y$ increases to $-0.10 \, \pi/b$, the parabolic-like band shifts up and the onset of the V-shape upper branch of the TSS band starts to appear [red arrow in Fig. 3(d)] that forms the Dirac-like cone at $\Gamma$ [Fig. 3(f)]. Cuts $10 \rightarrow 14$ [dashed vertical green lines in Fig. 3(a)] were taken along $k_y$ and are presented in Figs. 3(k)–3(o), with the corresponding value of $k_x$ marked on top of each panel. It is possible to notice that between $\pm 0.4 \, \pi/b$ the majority of the bulk bands have a parabolic shape, including the TSS at $\Gamma$. The red arrow in Fig. 3(m) shows the onset of the

formation of the TSS which has almost flat dispersion at $\Gamma$ along $k_y$.

Finally, we discuss the topological band structure of NiBi$_3$ which has symmetry operations in the space group 62 (Pnma) including inversion, a mirror plane along the $y$ axis, two glide planes along the $x$ and $z$ axes, and also three twofold screw axes along the three main axes. The bulk band structure of NiBi$_3$ has been calculated in experimental lattice parameters with PBE+SOC and is plotted in Fig. 4(a) with the high-symmetry $k$ points of the BZ. Because of the presence of both time-reversal symmetry (TRS) and inversion symmetry, each band has at least double degeneracy everywhere. Although the band dispersion on the planes of $k_z = 0.0 \, \pi/c$ ($S$-$Y$-$\Gamma$-$X$-$S$)

and $k_z = 1.0 \, \pi/c$ ($R$-$T$-$Z$-$U$-$R$) has resemblance over a large energy range, the dispersion along the $k_x$, for example $S$-$R$ and $\Gamma$-$Z$ directions, is still large. Thus, the band dispersion in NiBi$_3$ is only quasi-2D due to the small vacuum spacing of 1.6 Å between the stacked neighboring (Ni$_2$Bi$_6$) chain units. The top valence band, i.e., the $N$th band, highlighted in blue shows that there are multiple bands crossing the Fermi energy, indicating a complicated Fermi surface. Here $N$ stands for the number of electrons and the top valence band according to the simple band filling. However, for the symmetry analysis of the topological features, the most relevant band is band $N - 8$, which is highlighted in red. As enlarged in Fig. 4(b) along the $X$-$S$-$R$ direction, the band $N - 8$ forms fourfold crossings with the band $N - 6$. These crossings are part of a Dirac nodal loop on the $k_x = 1.0 \, \pi/a$ plane around the $S$ point and is protected by the glide plane perpendicular to the $x$ axis $\{m_x | 0, 1/2, 1/2\}$, which has been discussed previously for CaPtGa in the same space group 62 [37]. The shape of this Dirac nodal loop is shown by the contour of the bulk gap on the $k_x = 1.0 \, \pi/a$ plane in Fig. 4(c), indicating small and large spans along the $k_y$ and $k_z$ directions, respectively.

However, the observed surface Dirac point at $-0.185$ eV does not arise from the Dirac nodal loop, which is well below at $-1.0$ eV. To explain the origin of the surface Dirac point, the band $N - 8$ is also enlarged along the $Y$-$\Gamma$-$X$ direction in Fig. 4(d). Comparing to the surface spectral function in Fig. 2, it is clear that the surface Dirac point actually resides inside the bulk gap between the band $N - 8$ and the band $N - 6$. It is interesting that this section of the gap region along the $\Gamma$-$X$ direction remains open upon the bulk band projection from all the different $k_z$ values. Next, the parity eigenvalues ($n_+$ and $n_-$) at the time-reversal invariant momentum (TRIM) for the bands filled up to $N - 8$, a total of 68 accounting for the double degeneracy, have been calculated and tabulated in Fig. 4(f). The products of the parity eigenvalues at the TRIM are also labeled in the bulk BZ in Fig. 4(e), together with the schematic of the Dirac nodal loop on the $k_x = 1.0 \, \pi/a$ plane. Because of the gaplessness, the full 3D $Z_2$ index and diagnosis cannot be applied. Here the only gapless region is on the $k_x = 1.0 \, \pi/a$ plane due to the Dirac nodal loop. On the $k_z = 1.0 \, \pi/c$ plane with a well-defined bulk gap, the planar 2D $Z_2$ index can still be calculated as shown in Fig. 4(g) by the Wilson loop of the Wannier charge centers (WCC). The odd number of crossings for the horizontal dashed line with WCC in Fig. 4(g) shows the $k_z = 0.0 \, \pi/c$ plane is topologically nontrivial with $Z_2 = 1$, agreeing with the parity analysis in Fig. 4(e). To further confirm the surface Dirac point is topologically nontrivial, the spin texture of the surface states has been calculated and plotted on top of the isoelectronic surface at energy of $-0.21$ eV in Fig. 4(h), just below the Dirac point. It shows that the in-plane spin texture changes to the opposite direction when either $k_x$ or $k_y$ switches sign, which confirms the observed surface state crossing at energy of $-0.185$ eV is indeed a surface Dirac point and topologically protected by TRS. Thus, the symmetry analysis explains a rare combination of both a bulk Dirac nodal loop and surface Dirac point in NiBi$_3$.

From our study, we showed that NiBi$_3$ presents many bulk bands and SS that coexist near a Dirac-like state, which makes this system very complicated. Although the compound is a superconductor below $T_c = 4.1$ K, its electronphonon-mediated BCS nature gives rise a small gap of the order of 0.5 meV [15]. This, added to the fact that the TSS is located at high-binding energy, denies the topological superconductivity behavior on the surface at the Fermi level for NiBi$_3$. However, the saddle-like states suggest the existence of a van Hole singularity that, if tuned near to the Fermi level, could enhance interactions.

## IV. CONCLUSIONS

In summary, in this work we studied the bulk and topological band structure of the NiBi$_3$ using ARPES and DFT calculations. The crystal was cleaved perpendicular to the crystallographic $c$ axis and we were able to detect the bands along the $\Gamma$-$X$ direction. The reconstructed FS shows a complex structure with two very bright intensities around $\Gamma$ at $\pm 0.3 \, \pi/a$, followed by a sequence of broad Fermi sheets along $\Gamma$-$Y$. The band structure presents a TSS that forms a Dirac-like cone at $\Gamma$ with a surface Dirac point at the energy $-0.185$ eV. The surface state nature of this structure was investigated by ARPES, where it was measured using two different incident energies. The topological properties of NiBi$_3$ were discussed in terms of symmetry of the crystal structure and band structure. The 2D $Z_2$ index was calculated in the bulk gap region and the spin texture of the surface states were calculated for the Dirac cone. The results confirm that the surface state crossing observed at the $\Gamma$ point at $-0.185$ eV is a surface Dirac point and topologically nontrivial. As a function of the energy, the upper branch of the TSS forms a concave lens shape separated along $k_y$ that touches at the Dirac point. Remarkably, along $\Gamma$-$X$ the TSS shows a linear $X$-shape dispersion, while along the $\Gamma$-$Y$ direction presents saddle-like states with an almost flat region that collapses at the surface Dirac point. Furthermore, the calculated band structure presents a Dirac nodal loop at the $S$ point, and overall the calculated DFT matches the experimental data very well, especially for the TSS at the $\Gamma$ point.

[1] A. Isaeva, B. Rasche, and M. Ruck, Phys. Status Solidi **7**, 39 (2013).

[2] Y. L. Chen, J. G. Analytis, J.-H. Chu, Z. K. Liu, S.-K. Mo, X. L. Qi, H. J. Zhang, D. H. Lu, X. Dai, Z. Fang *et al.*, Science **325**, 178 (2009).

[3] Q. Jiang, D. Wang, Z. Liu, Z. Jiang, H. Qian, X. Shen, A. Li, D. Shen, S. Qiao, and M. Ye, Phys. Rev. B **104**, 245112 (2021).

[4] L. Fu and C. L. Kane, Phys. Rev. B **76**, 045302 (2007).

[5] Y. Liu and R. E. Allen, Phys. Rev. B **52**, 1566 (1995).

[6] A. K. Nayak, J. Reiner, R. Queiroz, H. Fu, C. Shekhar, B. Yan, C. Felser, N. Avraham, and H. Beidenkopf, Sci. Adv. **5**, eaax6996 (2019).

[7] M. Z. Hasan and C. L. Kane, Rev. Mod. Phys. **82**, 3045 (2010).

[8] A. P. Schnyder and P. M. R. Brydon, J. Phys.: Condens. Matter **27**, 243201 (2015).

[9] L. Fu and C. L. Kane, Phys. Rev. Lett. **100**, 096407 (2008).

[10] J. Alicea, Rep. Prog. Phys. **75**, 076501 (2012).

[11] M. S. Lee, C. M. Liu, and C. R. Kao, J. Electron. Mater. **28**, 57 (1999).

[12] G. Vassilev, V. Gandova, and P. Docheva, Cryst. Res. Technol. **44**, 25 (2009).

[13] C. Cruz, T. Lima, R. Kakitani, A. Barros, A. Garcia, and N. Cheung, J. Mater. Res. Technol. **9**, 4940 (2020).

[14] Y. Fujimori, S.-I. Kan, B. Shinozaki, and T. Kawaguti, J. Phys. Soc. Jpn. **69**, 3017 (2000).

[15] E. Gati, L. Xiang, L.-L. Wang, S. Manni, P. C. Canfield, and S. L. Bud'ko, J. Phys.: Condens. Matter **31**, 035701 (2019).

[16] J. Kumar, A. Kumar, A. Vajpayee, B. Gahtori, D. Sharma, P. K. Ahluwalia, S. Auluck, and V. P. S. Awana, Supercond. Sci. Technol. **24**, 085002 (2011).

[17] G. J. Zhao, X. X. Gong, P. C. Xu, B. C. Li, Z. Y. Huang, X. F. Jin, X. D. Zhu, and T. Y. Chen, Supercond. Sci. Technol. **31**, 125005 (2018).

[18] E. L. M. Piñeiroa, B. L. R. Herrera, R. Escudero, and L. Bucio, Solid State Commun. **151**, 425 (2011).

[19] B. Silva, R. F. Luccas, N. M. Nemes, J. Hanko, M. R. Osorio, P. Kulkarni, F. Mompean, M. García-Hernández, M. A. Ramos, S. Vieira, and H. Suderow, Phys. Rev. B **88**, 184508 (2013).

[20] P. Canfield, T. Kong, U. Kaluarachchi, and N. H. Jo, Philos. Mag. **96**, 84 (2016).

[21] R. Jiang, D. Mou, Y. Wu, L. Huang, C. D. McMillen, J. Kolis, H. G. Giesber, III, J. J. Egan, and A. Kaminski, Rev. Sci. Instrum. **85**, 033902 (2014).

[22] P. Hohenberg and W. Kohn, Phys. Rev. **136**, B864 (1964).

[23] W. Kohn and L. J. Sham, Phys. Rev. **140**, A1133 (1965).

[24] J. P. Perdew, K. Burke, and M. Ernzerhof, Phys. Rev. Lett. **77**, 3865 (1996).

[25] G. Kresse and J. Furthmuller, Phys. Rev. B **54**, 11169 (1996).

[26] G. Kresse and J. Furthmuller, Comput. Mater. Sci. **6**, 15 (1996).

[27] P. E. Blöchl, Phys. Rev. B **50**, 17953 (1994).

[28] H. J. Monkhorst and J. D. Pack, Phys. Rev. B **13**, 5188 (1976).

[29] N. Marzari and D. Vanderbilt, Phys. Rev. B **56**, 12847 (1997).

[30] I. Souza, N. Marzari, and D. Vanderbilt, Phys. Rev. B **65**, 035109 (2001).

[31] M. P. L. Sancho, J. M. L. Sancho, and J. Rubio, J. Phys. F: Met. Phys. **14**, 1205 (1984).

[32] M. P. L. Sancho, J. M. L. Sancho, and J. Rubio, J. Phys. F: Met. Phys. **15**, 851 (1985).

[33] Q. Wu, S. Zhang, H.-F. Song, M. Troyer, and A. A. Soluyanov, Comput. Phys. Commun. **224**, 405 (2018).

[34] I. Cucchi, A. Marrazzo, E. Cappelli, S. Riccò, F. Y. Bruno, S. Lisi, M. Hoesch, T. K. Kim, C. Cacho, C. Besnard *et al.*, Phys. Rev. Lett. **124**, 106402 (2020).

[35] N. F. Q. Yuan, H. Isobe, and L. Fu, Nat. Commun. **10**, 5769 (2019).

[36] K. Lee, G. F. Lange, L.-L. Wang, B. Kuthanazhi, T. V. Trevisan, N. H. Jo, B. Schrunk, P. P. Orth, R.-J. Slager, P. C. Canfield *et al.*, Nat. Commun. **12**, 1855 (2021).

[37] R. Chen, H. C. Po, J. B. Neaton and A. Vishwanath, Nature Phys **14**, 55 (2018).